

Electrical impedance myography method of measuring anisotropic tongue tissue

Xuesong Luo^{1,3}, Jian Shi², Arnau Marín Llobet³, Se-ward B. Rutkove⁴ and Benjamin Sanchez³‡

¹National Engineering Research Center of Neuromodulation, School of Aerospace Engineering, Tsinghua University, Beijing 100084, China

²Department of Automation Science and Electric Engineering, Beijing Advanced Innovation Center for Big Data-Based Precision Medicine, Beihang University, Beijing 100083, China

³Sanchez Research Lab, Department of Electrical and Computer Engineering, Sorenson Molecular Biotechnology Building, 36 South Wasatch Drive, University of Utah, Salt Lake City, UT 84112, USA

⁴Department of Neurology, Beth Israel Deaconess Medical Center, Harvard Medical School, Boston, MA 02245, USA

E-mail: shijian@buaa.edu.cn and benjamin.sanchez@utah.edu

Abstract. *Objective:* To date, measurement of conductivity and relative permittivity properties of anisotropic biological tissues using electrical impedance myography (EIM) is only possible through an invasive ex vivo biopsy procedure. Here, we present a novel forward and inverse theoretical modeling framework to estimate these properties combining surface and needle EIM measurements. *Methods:* The framework presented models the electrical potential distribution within a monodomain, homogeneous, and three-dimensional anisotropic tissue. Finite element method simulations and tongue experimental results verify the validity of our method to reverse-engineer three-dimensional conductivity and relative permittivity properties from EIM measurements. *Results:* FEM-based simulations confirm the validity of our analytical framework, with relative errors between analytical predictions and simulations smaller than 0.12% and 2.6% in a cuboid and tongue model, respectively. Experimental results confirm qualitative differences in the conductivity and the relative permittivity properties in x , y , and z directions. *Conclusion:* Our methodology enables EIM technology to reverse-engineer the anisotropic tongue tissue conductivity and relative permittivity properties thus unfolding full forward and inverse EIM predictability capabilities. *Significance:* This new method of evaluating anisotropic tongue tissue will lead to a deeper understanding of the role of biology necessary for the development of new EIM tools and approaches for tongue health measurement and monitoring.

Keywords: electrical impedance myography (EIM), electrical anisotropy, conductivity, relative permittivity.

‡ Corresponding author: Dr. Benjamin Sanchez, Sorenson Molecular Biotechnology Building, Office 3729, 36 South Wasatch Drive, University of Utah, Salt Lake City, UT 84112-9206, USA, phone: (801) 585-1494, email: benjamin.sanchez@utah.edu.

1. Introduction

Patients with neuromuscular disorders and researchers are in great need for improved biomarkers for disease care to assist with early diagnosis and to track disease progression over time and response to therapy, both for individual patient care and for clinical trials purposes. Electrical impedance myography (EIM) can serve as a biomarker to rapidly, quantitatively, and reliably diagnose and monitor diseased skeletal muscle at the bedside thus serving as tool to help tailor care for individual patients and to streamline and improve clinical drug trials (Rutkove 2009, Sanchez et al. 2021).

In EIM, a specific instance of broader bioimpedance field applied to muscle, a painless, alternating current is applied to the muscle tissue typically in the 1 kHz - 1 MHz range through a pair of current electrodes. The generated potential is then measured via a second pair of voltage electrodes (Sanchez et al. 2016, Rutkove et al. 2018). The most basic form of the technique is a surface measurement, in which single-frequency electrical current is typically applied through two surface electrodes and surface voltage measurements are made by two dedicated electrodes. There are more advanced approaches to EIM with needles, greater number of electrodes and multiple frequencies, thus allowing for a more focused approach to tissue assessment (Rutkove et al. 2018). By measuring the relationship between the current and the voltage, muscle reactance and resistance data are obtained (Sanchez & Rutkove 2017a, Sanchez & Rutkove 2017b, Rutkove & Sanchez 2018).

EIM is extremely sensitive to changes in muscle structure (Gillies & Lieber 2011) and composition, namely determined by the (electrical) admittivity property brought about by a variety of neuromuscular disorders, thus producing unique diseased resistance and reactance signatures that will vary with muscle status. In muscle for example, primary motor nerve diseases such as amyotrophic lateral sclerosis (ALS) will cause myofiber group atrophy (Kuwabara et al. 2008, Kim et al. 2009), and more chronically, reinnervation (Alix et al. 2020, Schooling et al. 2022). Primary muscle disease such as myopathies can be associated with varying degrees of edema (e.g., dermatomyositis) (Milisenda et al. 2014) followed by increasing connective tissue (Kharraz et al. 2014, Klingler et al. 2012) and fat deposition in the muscle (Liang & Nishino 2011, Toscano et al. 2017). Disuse atrophy, in contrast, is associated with mild degrees of fast-twitch fiber atrophy only (Wang & Pessin 2013).

Understanding how the admittivity impacts tongue EIM values over a range of neurological conditions affecting bulbar function remains an open challenge. As a result of the invasiveness associated to existing EIM methods based on biopsied tissue, there is still today a lack of scientific knowledge of the admittivity of living human tongue and their variation with gender, age, disease, anisotropy, or frequency of the electrical current. Broadly, most of the admittivity knowledge available today is limited to datasets collected on excised animal tissue samples gathered a few decades ago (Gielen et al. 1984, Faes et al. 1999) and, more recently, in diseased muscle (Nagy et al. 2019). Although clearly valuable, these ex vivo animal values are limited and can lead to divergent in vivo tongue EIM predictions from mathematical and computational models based on such values (Ganapathy & Clark 1987, Greco et al. 1977),

as they differ between species (e.g., due to fiber type slow- vs fast-twitch composition) and experimental conditions (e.g., temperature and tissue perfusion) between ex vivo and in vivo tissue (Klotz et al. 2020, Gielen et al. 1986, Opitz et al. 2017).

This work is framed by the technical challenge of reconstructing the anisotropic admittivity properties of tongue muscle from EIM data without requiring biopsying the tissue. Here, we develop an analytical reconstruction method to infer the conductivity and the relative permittivity properties of three-dimensional anisotropic tissue generating data collected via non-invasive surface and minimally-invasive needle EIM measurements. The method is validated performing finite element model simulations in a cuboid domain first and extended to human tongue model. We show experimental feasibility via a proof of concept study measuring ex vivo swine tongue.

2. Forward model in half and full space

2.1. Governing equation

We first pose the mathematical model that describes the passive, linear bioimpedance behavior of tissue considering an anisotropic tissue with three-dimensional admittivity property in an closed half three-dimensional Euclidean space $\mathbb{R}_-^3 := (x \in \mathbb{R}, y \in \mathbb{R}, z \in \mathbb{R}_{\geq 0})$ and full three-dimensional Euclidean space $\mathbb{R}^3 := (x \in \mathbb{R}, y \in \mathbb{R}, z \in \mathbb{R})$ shown in Figure 1 a and b, respectively. Henceforth, we hold the assumptions that electrodes are point-like and that there are no free charges in the tissue. Note zero free charges do not correspond to an absence of current. The charge responsible for the electric current in the tissue is determined by the external electrical current defined in the right hand side of (1). The concept and the implications of the assumption of point-like electrodes only exists and are limited to the definition of (1) and the solution of the reconstruction method presented. Then, the governing equation describing the macroscopic electrical behavior of tissue in the α and low-frequency β frequency range (Schwan 1984) in a homogeneous, monodomain tissue under half and full space assumptions $\Omega \in \{\mathbb{R}_-^3, \mathbb{R}^3\}$ is the generalized Poisson equation (Jargal et al. 2020)

$$\nabla \cdot \boldsymbol{\gamma} \nabla \mathbf{U}(\mathbf{r}) = -I \delta(\mathbf{r} - \mathbf{r}_S) \quad \text{in } \Omega, \quad (1)$$

where $\mathbf{r} = (x, y, z)^T$ is the vector of coordinates (m), T is the transpose operator, $\mathbf{U}(\mathbf{r}) \in \mathbb{C}$ (V) is the electrical potential distribution in Ω , $i := \sqrt{-1}$ (dimensionless) is the imaginary unit, $I \in \mathbb{R}$ (A) is the scalar amplitude of sinusoidal current at frequency ω_k generated by the source of electrical current S with coordinates $\mathbf{r}_S := (x_S, y_S, z_S)^T$ (m), the current sink is at infinity, $\mathbf{r} \neq \mathbf{r}_S$, $\omega_k := 2\pi f_k$ (rad s⁻¹) is the (angular) frequency f_k (Hz), $\delta(\cdot)$ is the Dirac delta function (m⁻³),

$$\boldsymbol{\gamma} := \text{diag}(\boldsymbol{\gamma}_x, \boldsymbol{\gamma}_y, \boldsymbol{\gamma}_z) = \begin{bmatrix} \boldsymbol{\gamma}_x & 0 & 0 \\ 0 & \boldsymbol{\gamma}_y & 0 \\ 0 & 0 & \boldsymbol{\gamma}_z \end{bmatrix},$$

diag is the diagonal matrix, $\boldsymbol{\gamma} \in \mathbb{C}_{3 \times 3}$ (S m⁻¹) is three-dimensional anisotropic admittivity property, and the admittivity in each direction is $\boldsymbol{\gamma}_{\{x,y,z\}} := \sigma_{\{x,y,z\}} + i\lambda_{\{x,y,z\}}$, subscripts

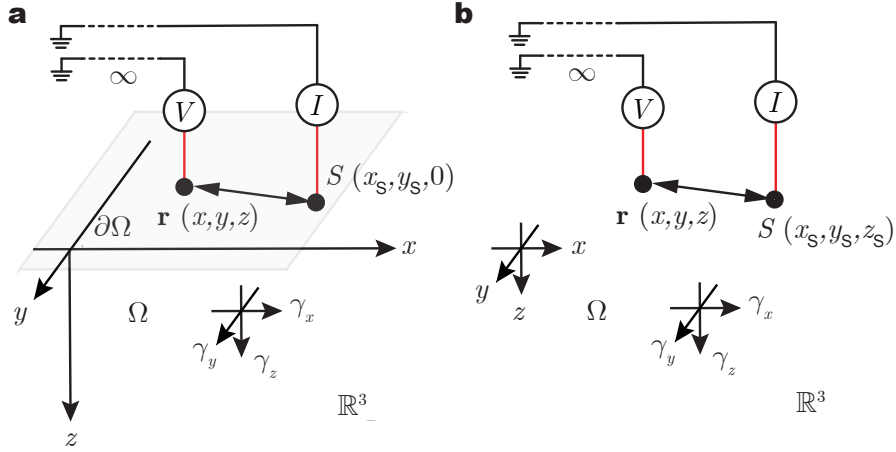


Figure 1. Schematic illustrating potential distributing model of three-dimensional anisotropic domain Ω in half (a) and full (b) space. The anisotropic admittivity is $\boldsymbol{\gamma}_{\{x,y,z\}}$ in x, y, z axis, respectively. The voltage recording electrode E is a point-like electrode with coordinates $\mathbf{r} := (x, y, z)$ in Ω . A point-like current source electrode S generates sinusoidal electrical current at $\mathbf{r}_S := (x_S, y_S, 0)$ on boundary $\partial\Omega := (x, y, 0)$ in (a); and then at $\mathbf{r}_S := (x_S, y_S, z_S)$ in (b). Note both current sink electrode and zero potential reference are located at infinity.

indicate x, y, z directions, $\sigma \in \mathbb{R}$ (S m^{-1}) is the electrical conductivity, $\lambda := \omega_k \epsilon_0 \epsilon_r$, ϵ_0 is the permittivity of vacuum, ϵ_r (dimensionless) is the relative permittivity.

In Cartesian coordinate system, governing equation (1) can be expanded into

$$\boldsymbol{\gamma}_x \frac{\partial^2 \mathbf{U}(\mathbf{r})}{\partial x^2} + \boldsymbol{\gamma}_y \frac{\partial^2 \mathbf{U}(\mathbf{r})}{\partial y^2} + \boldsymbol{\gamma}_z \frac{\partial^2 \mathbf{U}(\mathbf{r})}{\partial z^2} = -I \delta(\mathbf{r} - \mathbf{r}_S). \quad (2)$$

Of note, the half-space model (Figure 1 a) holds the additional boundary condition $(\partial \mathbf{U}(\mathbf{r}) / \partial z) |_{\partial\Omega} = 0$, where plane $\partial\Omega := (x, y, 0)^T$ is the boundary in tissue Ω in \mathbb{R}^3_- .

2.2. Electrical potential model

To solve (2) and find the general potential solution for the three-dimensional anisotropic case, we leverage our physical intuition combined with the Uniqueness theorem for Poisson's equation given the assumptions outlined in the previous Section. As shown in Lemma 1 in the Supplementary Material, the general equation of the electric potential distribution in three-dimensional anisotropic tissue and solution to (2) is

$$\mathbf{U}(\mathbf{r}) = \frac{I}{K \sqrt{\det(\boldsymbol{\gamma})}} \left((\mathbf{r} - \mathbf{r}_S)^T \boldsymbol{\gamma}^{-1} (\mathbf{r} - \mathbf{r}_S) \right)^{-\frac{1}{2}}, \quad (3)$$

where $\det(\cdot)$ is the determinant and

$$K := \begin{cases} 2\pi & \Omega \text{ in } \mathbb{R}^3_- \text{ and } z_S := 0 \\ 4\pi & \Omega \text{ in } \mathbb{R}^3 \end{cases}.$$

Equation (3) can be rewritten as

$$U = \frac{I}{K \sqrt{\boldsymbol{\gamma}_y \boldsymbol{\gamma}_z (x - x_S)^2 + \boldsymbol{\gamma}_x \boldsymbol{\gamma}_z (y - y_S)^2 + \boldsymbol{\gamma}_x \boldsymbol{\gamma}_y (z - z_S)^2}}. \quad (4)$$

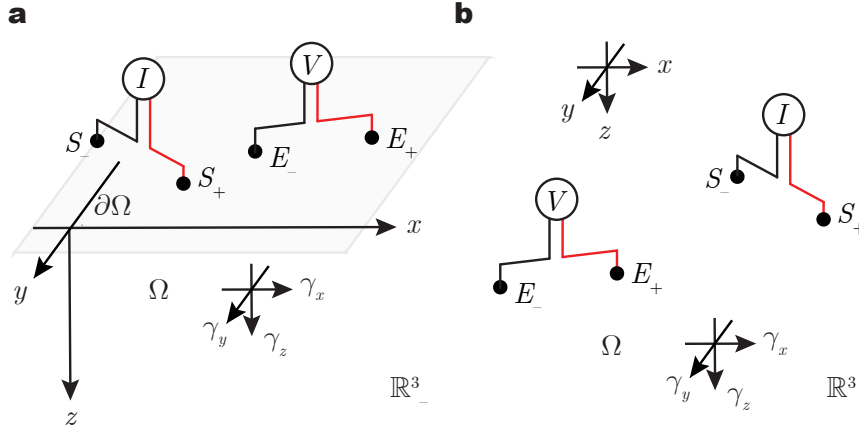


Figure 2. Tetrapolar impedance measurement of three-dimensional anisotropic tissue Ω in half (a) and full (b) space. The anisotropic admittivity is $\boldsymbol{\gamma}_{\{x,y,z\}}$ in x, y, z axis, respectively. High (+) and low (-) current source and sink electrodes are S_{\pm} , while high (+) and low (-) potential recording electrodes are E_{\pm} . Electrodes S_{\pm}, E_{\pm} are placed on the boundary $\partial\Omega$ in half space (a) and inside the tissue Ω in full space (b).

Equation (4) explicitly shows the spatial dependency of the potential with the admittivity properties in each direction. Note how the apparent admittance resulting from the square root in the denominator term weights the coordinates of a position with respect to the source with the tissue's three-dimensional admittivity properties in their perpendicular directions.

2.3. Bioimpedance model

Consider a four-electrode impedance measurement in Ω shown in Figure 2. Electrode S_+ and S_- represent the electrical current source and sink electrodes, respectively; whereas E_+ and E_- represent the high (+) and low(-) electrical potential recording electrodes, respectively. The apparent impedance $Z \in \mathbb{C}$ (Ohms) is

$$Z := \frac{(\mathbf{U}_{S_+}(\mathbf{r}_{E_+}) - \mathbf{U}_{S_-}(\mathbf{r}_{E_+})) - (\mathbf{U}_{S_+}(\mathbf{r}_{E_-}) - \mathbf{U}_{S_-}(\mathbf{r}_{E_-}))}{I}, \quad (5)$$

where \mathbf{U}_{S_+} and \mathbf{U}_{S_-} correspond to the electrical potential distribution generated by current source S_+ and sink S_- electrodes, respectively. Here, we use the term ‘‘apparent impedance’’ in lieu of just impedance or transfer impedance to explicitly denote the impedance measured accounts for the contribution of tissue anisotropic admittivity properties in three directions (see (4)). In general, the contribution of these anisotropic admittivity properties of tissue to the apparent impedance will change with the frequency measured as well as experimental factors such as the distance between EIM electrodes and their orientation with respect to the direction of anisotropy in the tissue. Substituting (3) in (5), one can obtain the expression of the apparent impedance in a three-dimensional anisotropic tissue.

Equation (5) can be further expanded by considering the four electrodes S_{\pm} and E_{\pm} are linearly aligned in half and full space (Figure 3 a and b, respectively). Length $A \in \mathbb{R}$ (m) is the distance between current and voltage electrodes, and $B \in \mathbb{R}$ (m) is the distance between

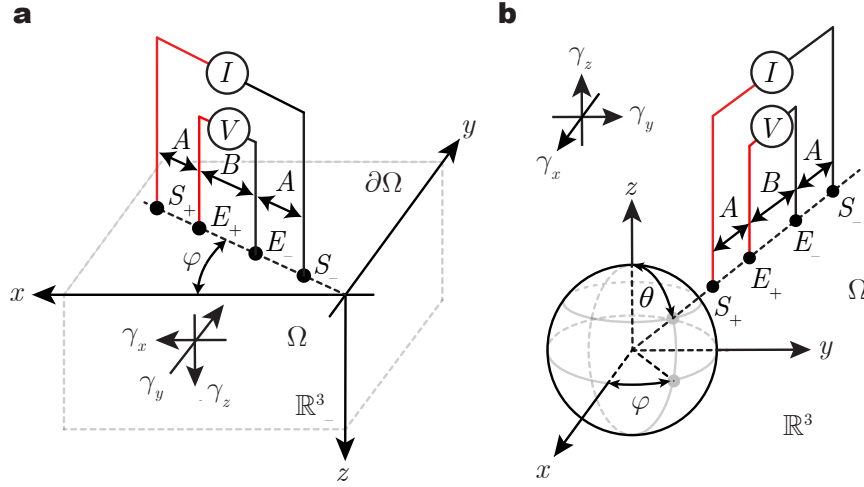


Figure 3. Linearly aligned electrodes measuring three-dimensional anisotropic impedance in half (a) and full (b) space. The anisotropic admittivity is $\gamma_{\{x,y,z\}}$ in x, y, z axes, respectively. High (+) and low (-) current source and sink electrodes are S_{\pm} , while high (+) and low (-) potential recording electrodes are E_{\pm} . Electrodes S_{\pm}, E_{\pm} are linearly aligned forming an angle θ with the z axis, while its projection on $x-y$ plane is defined by the angle φ with respect to the x axis. The distance between current and voltage electrodes is A , whereas the distance between the inner voltage recording electrodes is B . Electrodes S_{\pm}, E_{\pm} are placed on the boundary $\partial\Omega$ (i.e., $\theta = \pi/2$) in half space (a) and inside the tissue Ω in full space (b).

the inner voltage recording electrodes. According to (3) and (5), the apparent impedance is

$$Z = \frac{G}{K \sqrt{\gamma_z \sin^2 \theta (\gamma_y \cos^2 \varphi + \gamma_x \sin^2 \varphi) + \gamma_x \gamma_y \cos^2 \theta}}, \quad (6)$$

where $G := 2B/(A(A+B))$ is the geometrical coefficient (m^{-1}) determined by the relative positions of current and voltage electrodes, angle $\theta \in \mathbb{R}$ is the angle (rad) between z axis and the electrodes axis, angle $\varphi \in \mathbb{R}$ is the angle (rad) between x axis and the projection of electrodes' axis on $x-y$ plane. In the half-space model, $\theta = \pi/2$.

Of note, (6) can be further simplified if current and voltage electrodes are placed on the boundary $\partial\Omega$ in half space using surface electrodes for example, i.e., that is a non-invasive EIM measurement, namely

$$Z = \frac{G}{2\pi \sqrt{\gamma_y \gamma_z \cos^2 \varphi + \gamma_x \gamma_z \sin^2 \varphi}}. \quad (7)$$

Further, if we consider a full space measurement with current and voltage electrodes aligned with respect to the z axis for example using needles, then $\theta = 0^\circ$ and (6) becomes

$$Z = \frac{G}{4\pi \sqrt{\gamma_x \gamma_y}}. \quad (8)$$

3. Inverse model

Next, we provide an inverse modeling framework to evaluate the three-dimensional anisotropic admittivity based on a combination of non-invasive (surface, section 3.1) and minimally-invasive (needle, section 3.2) bioimpedance measurements using (7) and (8), respectively.

3.1. Half-space inverse surface model

3.1.1. Apparent bioimpedance measured in $M=2$ angles Consider the bioimpedance measurement where four linearly aligned electrodes are placed along the x and y axes in $M=2$ directions determined by the angles φ_1 and φ_2 , with $\varphi_1 := 0$ and $\varphi_2 := \pi/2$ rad as shown in Figure 3 a. Their averaged bioimpedance values $\hat{Z}_0, \hat{Z}_{\pi/2}$ are obtained via repeated bioimpedance measurements in each direction, i.e. $\hat{Z}_{\{0,\pi/2\}} := (1/N) \sum_{n=1}^N Z_{\{0,\pi/2\}}^{[n]}$ with $n = 2, 3, \dots, N$ and $N \in \mathbb{N}_{\geq 2}$. Then, $\mathbf{\Gamma}_{xz} := \gamma_x \gamma_z$ and $\mathbf{\Gamma}_{yz} := \gamma_y \gamma_z$ ($\text{S}^2 \text{ m}^{-2}$) can be estimated (denoted by the circumflex $\hat{}$) from (7) as

$$\hat{\mathbf{\Gamma}}_{yz} = \left(\frac{G}{2\pi\hat{Z}_0} \right)^2 \text{ and } \hat{\mathbf{\Gamma}}_{xz} = \left(\frac{G}{2\pi\hat{Z}_{\pi/2}} \right)^2. \quad (9)$$

3.1.2. Apparent bioimpedance measured in $M>2$ angles Here we extend the results from the previous section and consider a surface bioimpedance measurement in more than 2 angles. Consider all four electrodes linearly aligned on the surface of the half-space domain (Figure 3 a) where Z_1, Z_2, \dots, Z_M are the apparent impedance measured at angles $\varphi_1, \varphi_2, \dots, \varphi_M$, respectively, where $M \in \mathbb{N}_{>2}$ and $\hat{Z}_1, \hat{Z}_2, \dots, \hat{Z}_M$ are their averaged values over $N \in \mathbb{N}_{\geq 2}$ repeated measurements, i.e., $\hat{Z}_{\{1,2,\dots,M\}} := (1/N) \sum_{n=1}^N Z_{\{1,2,\dots,M\}}^{[n]}$ with $n = 2, 3, \dots, N$. According to (7), $\mathbf{\Gamma}_{yz}$ and $\mathbf{\Gamma}_{xz}$ can be estimated in a linear-least square sense as follows

$$\begin{bmatrix} \hat{\mathbf{\Gamma}}_{yz} \\ \hat{\mathbf{\Gamma}}_{xz} \end{bmatrix} = (\mathbf{A}^T \mathbf{W} \mathbf{A})^{-1} \mathbf{A}^T \mathbf{W} \mathbf{b}, \quad (10)$$

where $\mathbf{A} := \begin{bmatrix} \cos^2 \varphi_1 & \sin^2 \varphi_1 \\ \cos^2 \varphi_2 & \sin^2 \varphi_2 \\ \vdots & \vdots \\ \cos^2 \varphi_M & \sin^2 \varphi_M \end{bmatrix}$, $\mathbf{b} := \begin{bmatrix} (G/(2\pi\hat{Z}_1))^2 \\ (G/(2\pi\hat{Z}_2))^2 \\ \vdots \\ (G/(2\pi\hat{Z}_M))^2 \end{bmatrix}$ and \mathbf{W} is a user-defined weight matrix with positive elements (e.g., optimization-based to ensure robustness to experimental noise).

3.2. Full-space inverse needle-based model

Consider the minimally invasive measurement setup illustrated in Figure 3 b with $\theta = 0$, where all four electrodes are linearly aligned parallel to the z axis. According to (8), it follows

$$\widehat{\Gamma}_{xy} = \left(\frac{G}{4\pi\widehat{Z}} \right)^2. \quad (11)$$

where $\Gamma_{xy} := \gamma_x \gamma_y$ ($\text{S}^2 \text{ m}^{-2}$), $\widehat{Z} := (1/N) \sum_{n=1}^N Z^{[n]}$, $n = 2, 3, \dots, N$ and $N \in \mathbb{N}_{\geq 2}$ is the number of repeated measurements.

3.3. Three-dimensional anisotropic admittivity reconstruction

The three-dimensional anisotropic admittivity can be computed combining (10) and (11), namely

$$\begin{cases} \widehat{\gamma}_x = \sqrt{\widehat{\Gamma}_{xy} \widehat{\Gamma}_{xz} / \widehat{\Gamma}_{yz}} \\ \widehat{\gamma}_y = \sqrt{\widehat{\Gamma}_{xy} \widehat{\Gamma}_{yz} / \widehat{\Gamma}_{xz}} \\ \widehat{\gamma}_z = \sqrt{\widehat{\Gamma}_{xz} \widehat{\Gamma}_{yz} / \widehat{\Gamma}_{xy}}. \end{cases} \quad (12)$$

4. Materials and methods

4.1. Finite element method forward potential simulations in half- and full-space

The analytical forward electrical potential solution was first validated at 50 kHz using Comsol Multiphysics (Comsol, Inc., Burlington, MA, USA) via FEM simulations in the cuboid domain shown in Figure 4. The half- and full-space forward potential model simulated in the cuboid domain had a point-like current source electrode S positioned at the center of top surface (Figure 4 a) or the central area (Figure 4 b) for half- and full-space simulations, respectively, with current sink and potential reference at the opposite sides. The component of the electric current normal to all the outer boundaries was defined to be null to prevent the current flowing out of the boundaries defined by the model. The cuboid dimensions were $5 \cdot 10^4 \text{ mm} \times 5 \cdot 10^4 \text{ mm} \times 2.5 \cdot 10^4 \text{ mm}$ for half space (Figure 4 a, c) and $5 \cdot 10^4 \text{ mm} \times 5 \cdot 10^4 \text{ mm} \times 5 \cdot 10^4 \text{ mm}$ for full space (Figure 4 b, d). Note we simulated this domain intentionally to accurately validate our new theory obtained in infinity half/full space without the influence of boundary conditions. The anisotropic conductivity and the anisotropic relative permittivity in x, y and z directions were set to 1, 2 and 4 S m^{-1} and $2 \cdot 10^5$, $3 \cdot 10^5$, and $5 \cdot 10^5$ dimensionless, respectively. The number of discretized elements were 84,814 and 143,110 for the half- and full-space models, respectively.

4.2. Finite element method forward EIM simulations in a human tongue model

Half- and full-space forward potential simulations were then extended to generate EIM data necessary to evaluate the inference method presented here for reconstructing the anisotropic

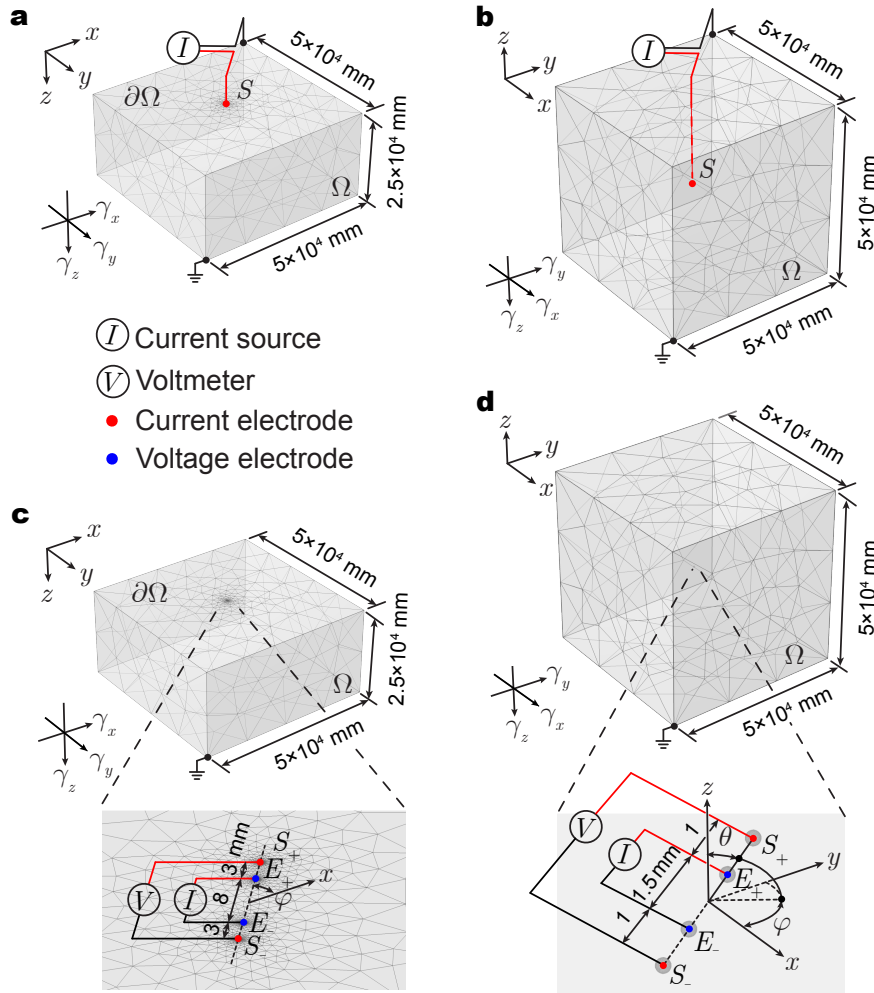


Figure 4. Electrical potential (a, b) and impedance (c, d) simulation in anisotropic box domain. Admittivity $\gamma_x, \gamma_y, \gamma_z$ are electrical property in x, y, z axis, respectively. A finite element model (FEM) Ω is built in a $5 \cdot 10^4 \text{ mm} \times 5 \cdot 10^4 \text{ mm} \times 2.5 \cdot 10^4 \text{ mm}$ region as half space (a, c) and in a $5 \cdot 10^4 \text{ mm} \times 5 \cdot 10^4 \text{ mm} \times 5 \cdot 10^4 \text{ mm}$ region as full space (b, d). In potential FEM, point-like current source S is placed on the surface $\partial\Omega$ (a) and in the center (b) of model region, with sink and reference potential at opposite vertexes of box domain. In impedance FEM, linearly aligned dimensionless electrodes S_{\pm} and E_{\pm} are source/sink and high/low potential recording electrodes. Their direction has an angle θ with the z axis, while its projection on $x - y$ plane is defined by the angle φ with respect to the x axis. Four electrodes are on the surface $\partial\Omega$ in half space (c) with $|E_+E_-| = 8 \text{ mm}$, $|S_+E_+| = |S_-E_-| = 3 \text{ mm}$, and in the center of full space (d) with $|E_+E_-| = 1.5 \text{ mm}$, $|S_+E_+| = |S_-E_-| = 1 \text{ mm}$. The component of the electric current normal to all the outer boundaries was defined to be null to prevent the current flowing out of the boundaries defined by the model. $|E_+E_-|, |S_+E_+|, |S_-E_-|$ are the distances between electrodes S_{\pm} and E_{\pm} respectively.

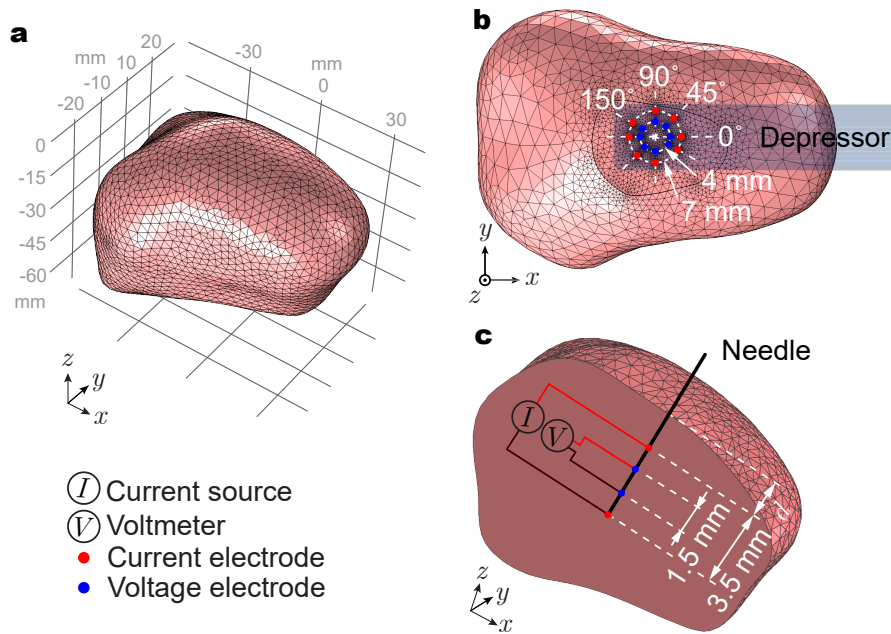


Figure 5. (a) Three-dimensional view of the human tongue finite element model (FEM) simulated. (b) Top view of non-invasive dimensionless measurement with the tongue depressor. (c) Sagittal cross section to illustrate the placement of a tetrapolar needle dimensionless inserted into the tongue with depth d . The component of the electric current normal to all the outer boundaries was defined to be null to prevent the current flowing out of the boundaries defined by the model.

admittivity properties of a human tongue FEM model. For this, we simulated the human tongue model shown in Figure 5. Non-invasive surface and minimally-invasive needle forward bioimpedance models are illustrated in Figure 5. Point-like source S_+ and sink S_- current and voltage measuring high E_+ and low E_- electrodes were linearly aligned on the top surface of the tongue (Figure 5 b) and vertically inserted into the tongue (Figure 5 c). Surface bioimpedance FEM simulations emulated the dimensions of our tongue electrode depressor with sixteen electrodes oriented in 4 directions (i.e., 0° , 45° , 90° , 150°) as shown in Figure 5 b with the same boundary conditions as in Section 4.1. In vivo human tongue admittivity values in x and y axis were taken from our previous clinical study (Luo et al. 2021a). The admittivity in z axis was defined as the geometrical mean in x and y direction. We simulated the model at 8, 16, 32, 64, 128, and 256 kHz considering a sinusoidal current of amplitude 1 mA. To discretize the tongue model, we used adaptive meshing where the maximum and minimum mesh element size was 10 and 10^{-3} mm, respectively. The maximum element growth rate is configured as 1.4 and the curvature factor is 0.2, resulting in a total of 465,848 elements.

4.3. Needle electrode characterization

Small electrodes can result in measurement artefacts. For this reason, we conducted first an impedance characterization of the needle electrodes used in this study. Electrode impedance measurements of needle EIM used during tongue experimentation were performed with the

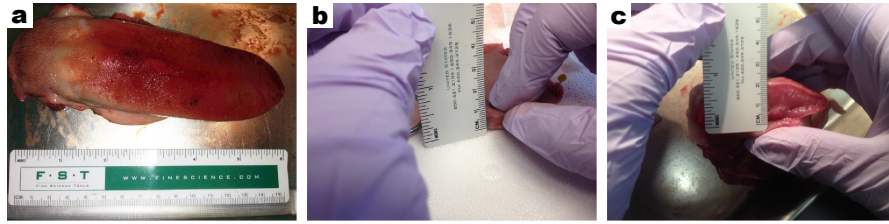


Figure 6. Representative images from the ex vivo tongue experimentation.

needle suspended in air using a micromanipulator and immersed in phosphate buffered saline solution (1xPBS, pH 7.4, Gibco™). Electrical impedance measurements were performed at room temperature using a high precision impedance analyzer (MFIA, Zurich Instruments, Zurich, Switzerland) at 10 kHz with a 50 mV sinusoidal amplitude.

4.4. Tissue experimentation: tongue preparation

As proof of concept and to show experimental feasibility, we measured three-dimensional conductivity and relative permittivity properties on ex vivo tongue from $N = 2$ pigs immediately after sacrifice. For the purposes of confirming the validity of our approach, each experiment was performed on a different day. Although such tissue is no longer living, the anisotropic characteristics of the tissue persists since the muscle fibers themselves remain largely intact, even 2 weeks after slaughter (Taylor & Koohmaraie 1998). Throughout the experiment, the tongue was gently moistened with gauze soaked in 0.9% normal saline at room temperature. For each experiment, a total of 5 repeated measurements were performed to obtain the mean value of the conductivity and the relative permittivity properties along the x, y, z axes.

4.5. Surface and needle electrodes for EIM measurements

Surface bioimpedance measurements were performed our recently developed tongue array described in our previous theoretical and experimental studies (Luo et al. 2021a, Luo et al. 2021b, Luo & Sanchez 2021), we refer the reader to these studies for further technical information. Briefly, the tongue electrode depressor consists of 16 point-like electrodes arranged at $0^\circ, 45^\circ, 90^\circ, 150^\circ$. The radii from current (outer) and voltage (inner) electrodes to array center are 7 and 4 mm, respectively. For invasive measurements, we used a tetrapolar EIM needle also described in (Rutkove et al. 2022) and manufactured by Haystack Diagnostics, Inc. (Lowell, MA). The distance between current and voltage electrodes are 3.5 and 1.5 mm, respectively, with an electrode area of 1.137 mm^2 . Electrodes were inserted 5 mm in the dorsum of the tongue as measured with a vernier caliper. For the surface bioimpedance measurements, we repositioned the tongue array in between repeated measurements. For the needle bioimpedance measurements, we intentionally did not reposition the needle in between repeated measurement to prevent tissue damage.

4.6. Impedance analyzer

The MFIA was used for ex vivo swine tongue bioimpedance measurements. The frequency of applied current f_k ranged from 10 to 1,000 kHz, with k the frequency index $k = \{1, \dots, F\}$, and $F = 100$ the number of frequencies distributed logarithmically within the frequency range.

4.7. Data analysis: inference method

The electrodes' spacing and direction along with FEM simulated and experimentally measured apparent surface and needle tongue bioimpedance values were used to infer the three-dimensional anisotropic admittivity properties using MATLAB (The MathWorks, Natick, MA).

5. Simulation results

The purpose of FEM forward and inverse simulations in a cuboid domain described in Sections 5.1 to 5.3 is to validate numerically the accuracy of the analytical model considering the assumptions on which the inference method has been developed for. The impact of the finite size and shape of the domain are then numerically evaluated by considering a computational model based on a realistic human anatomical model of the tongue in Section 5.4.

5.1. Forward potential distribution in a cuboid domain

Figure 7 shows analytical and FEM simulated electrical potential results at 50 kHz for models shown in Figure 4 a and b. The isopotential lines and current density distribution are shown in the xz , yz , xy planes in half- (Figure 7 a, model shown in Figure 4 a) and full-space (Figure 7 c, model shown in Figure 4 b) domains. Note the anisotropic nature of the admittivity generates ellipsoidal isopotential lines within the domain (Figure 7 a and c). The agreement between analytical (2) and FEM model predicting potential is excellent in both half (Figure 7 b) and full (Figure 7 d) space cases, with a maximum relative errors $< 0.15\%$ and $< 0.08\%$, respectively.

5.2. Forward EIM data in a cuboid domain

Analytical and FEM simulated forward resistance and reactance are compared in Figure 8 a and b in half-space according to (7) and full-space according to (6) for models shown in Figure 4 c and d, respectively. As expected in anisotropic tissue, apparent EIM values change with θ and φ angles. The agreement between forward analytical and FEM resistance and reactance simulated values is excellent with a maximum relative errors $< 0.12\%$ and $< 0.07\%$ in half- and full-space, respectively.

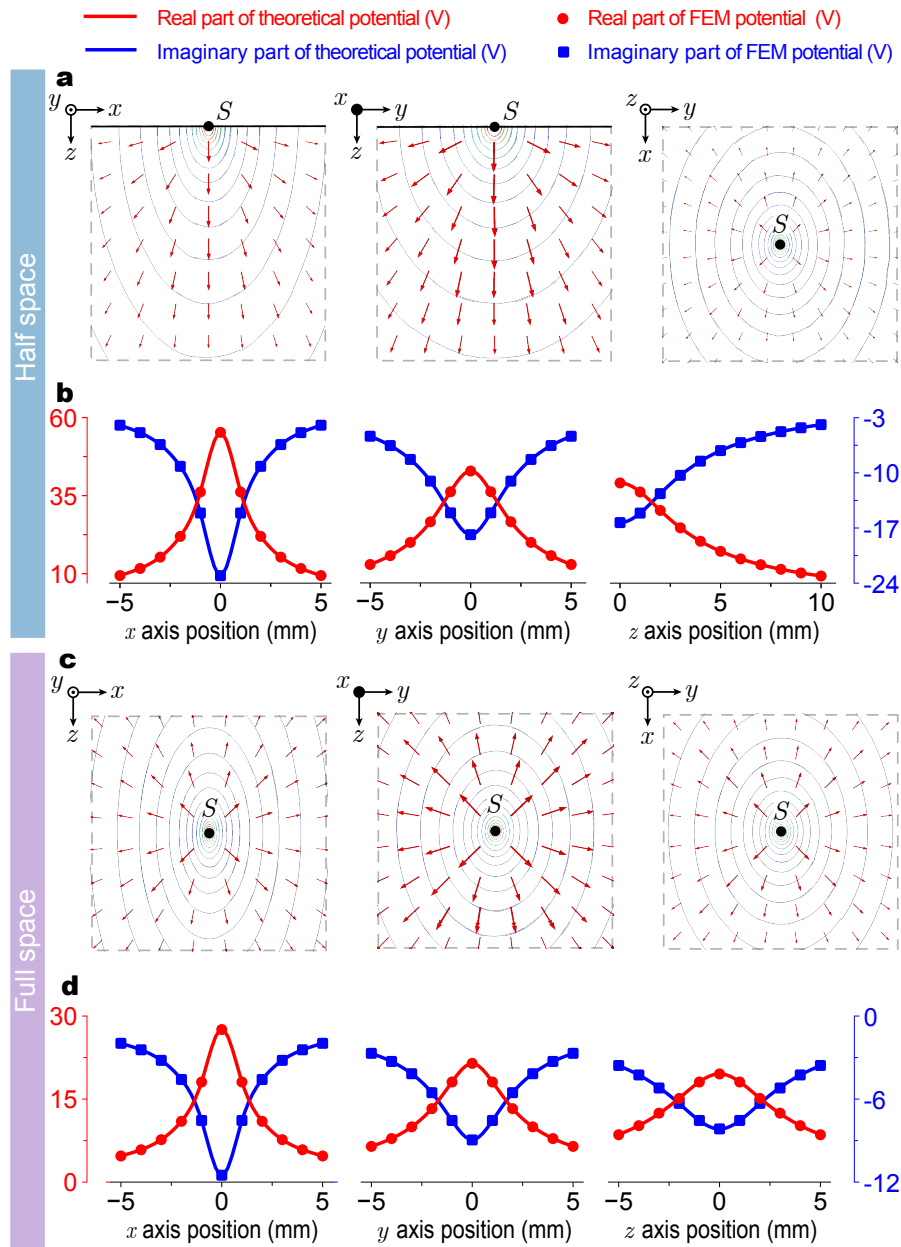


Figure 7. Analytical (2) and FEM-simulated electrical potential results in a cuboid domain at 50 kHz. Analytical and FEM isopotential lines, current density field, and electrical potential results shown were generated considering a current source S located at the origin of coordinates $x = y = z = 0$ m. The real (red, circle) and imaginary (blue, square) part of theoretical (solid lines) and FEM (symbols) electric potential in V for half-space (b) and full-space (d) are plotted changing the position of the voltage measuring electrode with $y = z = 1$ mm and with $x = [-5, 5]$ mm (left), $x = z = 1$ mm and with $y = [-5, 5]$ mm (center), and $x = y = 1$ mm and with $z = [0, 5]$ mm and $z = [-5, 5]$ mm (right). The conductivity and relative permittivity in x, y, z direction are $1, 2, 4 \text{ S m}^{-1}$ and $2 \cdot 10^5, 3 \cdot 10^5, 5 \cdot 10^5$ (dimensionless), respectively.

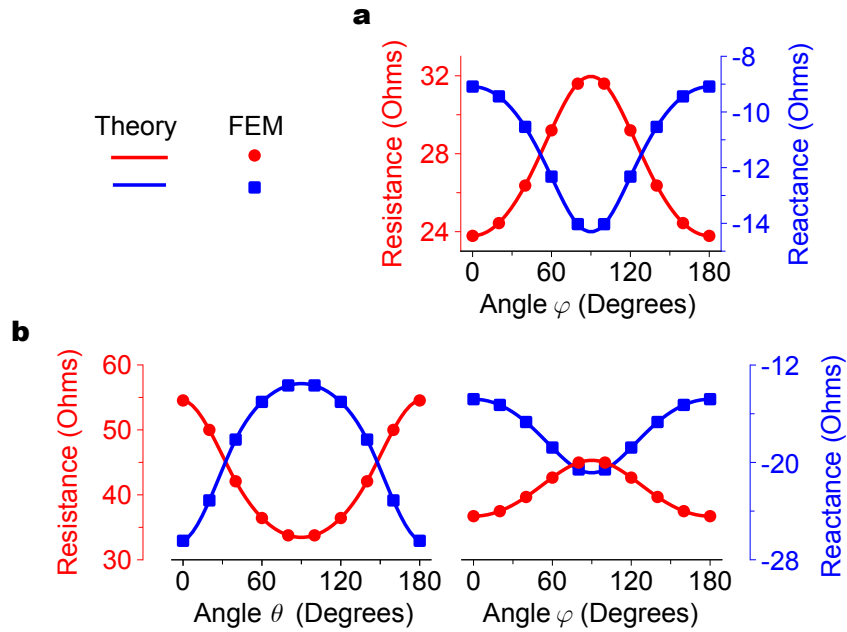


Figure 8. Forward analytical and FEM-simulated data generated in a cuboid domain simulating non-invasive (7) (a) and minimally-invasive (6) (b) EIM measurement at 50 kHz. Theoretical (solid lines) resistance (in red) and reactance (in blue) are compared to FEM (circle and square) values in half-space (a) with $\varphi = [0^\circ, 180^\circ]$, and full-space (b) with $\theta = [0^\circ, 180^\circ]$ and $\varphi = 45^\circ$, and $\varphi = [0^\circ, 180^\circ]$ and $\theta = 45^\circ$. The simulating parameters of conductivity and relative permittivity setting in x, y, z axial direction are 1, 2, and 4 S m^{-1} and $2 \cdot 10^5$, $3 \cdot 10^5$, and $5 \cdot 10^5$ dimensionless, respectively. The geometrical setting are $A = 3 \text{ mm}$, $B = 8 \text{ mm}$ in half space, and $A = 1 \text{ mm}$, $B = 1.5 \text{ mm}$ in full space.

5.3. Inverse admittivity reconstruction in a cuboid domain

Figure 9 shows the admittivity inferred from the FEM simulated forward EIM data generated in section 5.2 using (12) with \mathbf{W} the identity matrix and compared to the true values inputted into the FEM model. The reconstruction method provides accurate admittivity results with a maximum relative error $< 0.14\%$ at 50 kHz the simulated frequency.

5.4. Admittivity reconstruction of FEM simulated human tongue EIM values

Figure 10 compares the inferred admittivity against the ground truth admittivity values used in our tongue FEM simulations at different frequencies. Figure 10 shows the reconstruction errors are larger when the needle electrodes are close to the surface of the tongue and vice versa. The deeper the needle is inserted, the farther the electrodes from the tongue boundary are and the smaller the reconstructing error is. We found that when the depth is 4 mm, the relative reconstructing error was smaller than 2.6%.

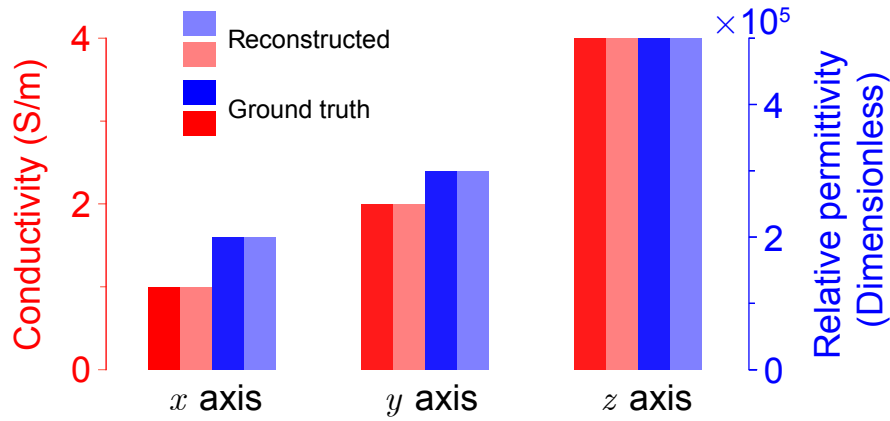


Figure 9. Anisotropic admittivity reconstructed in the cuboid domain combining non-invasive and invasive EIM data generated at 50 kHz. The inferred admittivity is then compared with FEM ground truth values.

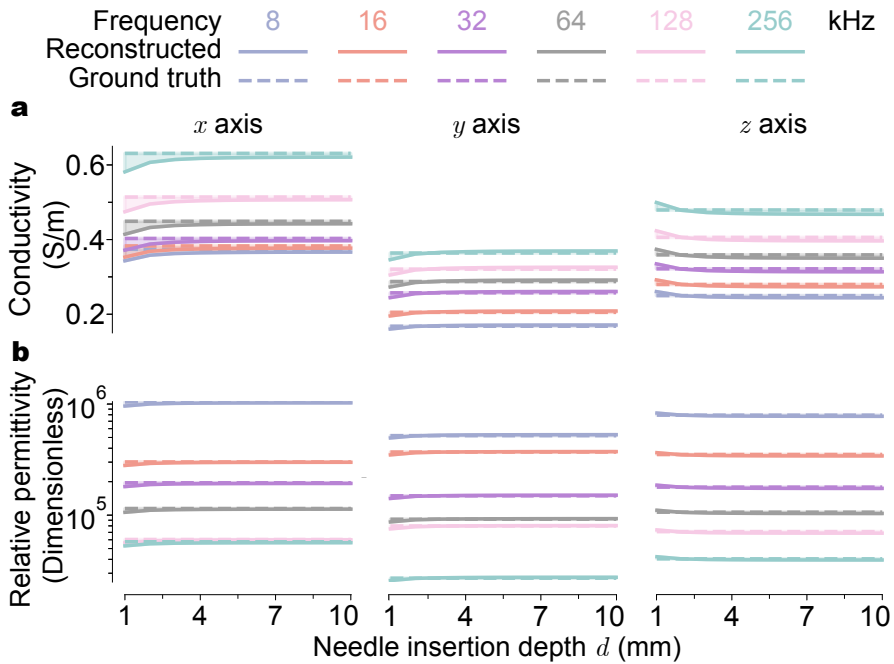


Figure 10. Comparison of reconstructed and FEM ground truth tongue conductivity (a) and relative permittivity (b) values at selected simulated frequencies $f_k = \{8, 16, 32, 64, 128, 256\}$ kHz. The reconstructed admittivity (solid line) is estimated by combining invasive and non-invasive forward tongue bioimpedance data. Needle bioimpedance values were simulated with the depth d changing from 1 to 10 mm.

Table 1. Characterization of electrodes used for intramuscular tongue needle EIM measurement in saline solution and air at 10 kHz.

	Saline solution	Air
Magnitude (k Ω)	0.6	399.8
Phase ($^{\circ}$)	-17	-86
Resistance (k Ω)	0.5	27.8
Capacitance (nF)	91.2	0.0004

6. Experimental results

The experimental results show proof of concept of the reverse method presented. First, we perform an experimental characterization of the electrodes in Section 6.1 followed by Section 6.2 to show experimental feasibility reconstructing tongue anisotropic admittivity values from ex vivo swine tongue EIM measurements.

6.1. Needle electrode impedance characterization

We performed bench testing of the needle EIM electrodes used for intramuscular tongue recordings to determine electrodes' impedance values. This studies included air and saline solution measurements at room temperature. Table 1 summarizes the impedance contact values (magnitude, phase, resistance, and capacitance) for the needle EIM.

6.2. In situ tongue conductivity and relative permittivity data

Multi-frequency conductivity and relative permittivity data reconstructed from ex vivo tongue EIM measurements are shown in Figure 11 a and b, respectively. These values were reconstructed using (12) with \mathbf{W} the identity matrix. To obtain a measure of variability in the data, we averaged the standard error of the mean for each dataset across the frequencies measured. The average standard error of the mean across the frequency range is $3.6 \cdot 10^{-4}$, $2.4 \cdot 10^{-4}$, and $1.7 \cdot 10^{-4}$ S m $^{-1}$ for the conductivity in x , y , and z axis, respectively; and 38.7, 54.6, and 29.5 (dimensionless) for the relative permittivity in x , y , and z axis, respectively. Qualitatively, the results indicate that our inverse method consisting of a combination of non-invasive surface and minimally-invasive needle EIM measurements can reconstruct the anisotropic admittivity property in the intrinsic musculature of the tongue consisting of transversely, longitudinally and vertically-aligned oriented myofibers. In the range of frequencies measured, averaged tongue conductivity and the relative permittivity values show a monotone increasing and decreasing frequency dependence, a result that is consistent with the frequency dependence of biological tissues at the range of frequencies measured (Schwan & Kay 1957, Duck 1990).

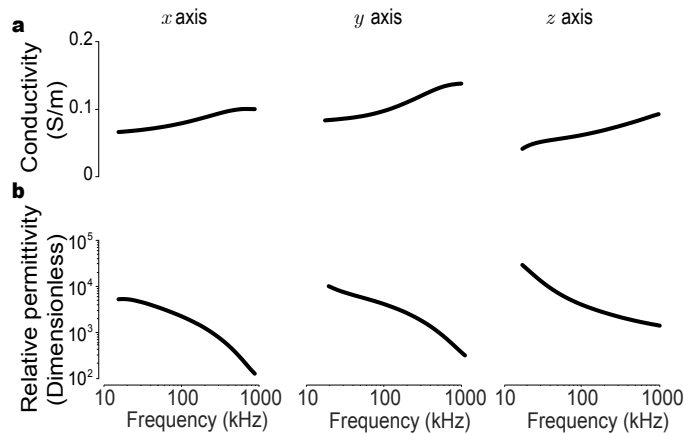


Figure 11. Reconstructed three-dimensional anisotropic conductivity (a) and relative permittivity (b) properties from $N = 2$ ex vivo swine tongue at measured frequencies from 10 kHz to 1 MHz. Values shown represent the mean value obtained from 10 bioimpedance measurements.

7. Discussion

Here, we have developed an *analytical* method to obtain determinations of the conductivity and relative permittivity properties of three-dimensional anisotropic tongue tissue. The inverse method presented relies on a combination of noninvasive and minimally-invasive EIM measurements in direct contact with the muscle of interest. This can be achieved when measuring the tongue which, unlike appendicular muscles, is not hidden underneath subcutaneous fat tissue. By combining a non-invasive surface and minimally-invasive needle EIM measurement approaches, it is then possible to obtain the same number of degrees of freedom as the number of unknowns in the final reconstruction of three-dimensional anisotropic admittivity property of tongue tissue. The method has been formally validated through a virtuous simulation cycle performing exhaustive analytical and finite element model simulations considering a cuboid domain as well as a realistic human tongue model. Finally, we performed proof of principle experiments to infer the anisotropic admittivity of ex vivo swine tongue, the primary tissue for which the new method has been developed.

State-of-the-art *computational* methods to invert EIM data and reconstruct anisotropic human muscle admittivity data such as the one described in (Kangasmaa & Laakso 2022) represent a challenging task whose cost is mainly due to the need of prior magnetic resonance imaging (MRI) as well as labor-intensive tissue segmentation and model reconstruction. Kangasmaa and Laakso used MRI-generated subject-specific computer models to solve numerically the forward electrostatic problem. To estimate the *two-dimensional* anisotropic *conductivity* values from experimental EIM data, the authors used a nonlinear minimization problem to minimize the misfit between simulated and measured EIM data but did not include regularizing constraints to improve stability, convergence and robustness to modeling errors and measurement noise (equation 4 therein). By iteratively updating the simulated admittivity values with a brute force algorithm, the difference between simulated EIM data and actual

experimental EIM data was minimized, effectively fitting the model to the measured data. It is worth to note the authors did not reconstruct *three-dimensional conductivity and relative permittivity* values albeit they measured both resistance and reactance.

Computational methods based on combining MRI and FEM simulation data as the one described above are advantageous since they allow to parameterize realistically the shape of muscle to then estimate non-invasively in vivo anisotropic admittivity values; but, at the same time, this approach has clinical and technical limitations that hinder its widespread use in patients with neuromuscular disorders. Clinical limitations associated with the use of MRI in this population include: 1. the requirement that individuals must go to a specialized facility for testing; 2. it cannot be used in young children without sedation; 3. subjects must lie flat, a major problem in neuromuscular patients with respiratory compromise; 4. it cannot be used in patients with certain implanted medical devices; 5. it is costly to perform; 6. only one body region can be scanned at a time and cannot assess short-term real-time admittivity changes of muscle with contraction; 7. the test is slow, typically taking 45 minutes or longer to perform. This limits its application in the electrodiagnostic clinic because the results are always generated offline by intensive image and computation post-processing and not in real time. Technically, due to the ill-posedness of the nonlinear inverse problem, additional terms are needed in the minimization to ensure the well-posedness in the presence of noise and/or inadequate measurements (Adler & Boyle 2019, Jauhiainen et al. 2020). Also, these optimization methods often suffer from local minima because of nonlinearity (Hamilton et al. 2019), so there is no absolute certainty that the admittivity found is biologically correct and it can only be contrasted qualitatively against literature values, just like the authors did in (Kangasmaa & Laakso 2022).

An alternative approach consists of developing computationally efficient *analytical* inverse measurement methods as in (Rush 1962, Rush et al. 1963, Kwon et al. 2017, Kwon, Guasch, Nagy, Rutkove & Sanchez 2019). To date, however, the existing analytical methods we have developed only allow to reconstruct the admittivity property of two-dimensional anisotropic tissue (Kwon, de Morentin, Nagy, Rutkove & Sanchez 2019). Here, we expanded the two-dimensional inverse reconstruction to solve the three-dimensional anisotropic case. The gist of our approach to solve the governing equation (1) is to use the method of analytic continuation to develop the three-dimensional anisotropic forward potential expression from the well-known isotropic potential equation directly (Teixeira & Chew 1997). As for the compatibility of our forward model, note the theoretical framework presented can easily degenerate back to the two-dimensional case just by setting two directions with the same admittivity (not shown).

To perform in vivo tongue admittivity measurements in the clinic, we envision in future work to combine both our non-invasive tongue depressor and multi-electrode needle devices described in (Rutkove et al. 2022, Luo et al. 2021a, Luo et al. 2021b). Through separate research and commercialization efforts, we have now been able to manufacture a 26-gauge multi-electrode needle that conforms to the standard dimensions of commercially available needles used in an electromyography test. We foresee tongue needle EIM examination using such multi-electrode needle being performed similarly to current tongue needle

electromyography studies as patient standard of care (Finsterer et al. 1997, Tankisi et al. 2013).

This work has several limitations. First, both the forward and inverse methods assume an infinitely large tissue. In practice, tissues and tongue specifically have limited size including irregular shape. Second, the method requires a minimally-invasive needle EIM measurement. Our simulation results suggest a minimum needle depth of insertion of 4 mm to minimize reconstruction errors due to boundary effects. Third, we assumed the needle's voltage and current electrodes can be placed without positioning errors in the z direction. A more robust model should consider an unknown experimental angle between the electrodes' linear axis and the anisotropic tissue direction along this axis. Also, the method presented is based on the assumption of point-like electrodes whereas in practice they have a finite size. The size of the electrodes will involve instrumentation considerations in practice to ensure experimental data accuracy with contact impedances at the electrode-tissue interface. Finally, the experimental data were not contrasted against the standard based on a tissue sample measured in a dielectric cell (Sanchez et al. 2014), since the objective of our measurements here is not to provide reference data but to demonstrate the viability of the method proposed. These limitations will be addressed in future work.

8. Conclusions

This study is the first to propose a forward and inverse analytical method to reconstruct three-dimensional anisotropic admittivity property from tongue EIM measurements. Broadly, enhancing our understanding of the interplay between EIM and the governing tissues' anisotropic admittivity property will provide unique insights into our interpretation of diseased tissue. This newly gathered knowledge will find vast use in mathematical calculations of electric fields and it will lead to a deeper understanding of the role of tissue structure and composition in the propagation of electricity within anisotropic tissue. The method presented of evaluating tissues' anisotropic permittivity will also be of great benefit in developing new translational EIM technologies for diagnosing diseased tongue tissue and tracking changes over time in patients with bulbar dysfunction.

Conflict of interest

Dr. Rutkove has equity in and serves a consultant and scientific advisor to Myolex, Inc., and Haystack Diagnostics, Inc., companies that design impedance devices for clinical and research use; he is also a member of the Myolex's Board of Directors. The companies also have an option to license patented impedance technology of which Dr. Rutkove is named as an inventor.

Dr. Sanchez holds equity and serves as scientific advisor in Haystack Diagnostics, Inc., and the company has an option to license patented needle impedance technology where the author is named an inventor. He also holds equity and serves as Scientific Advisory Board Member of Ioniq Sciences, Inc., a company that develops clinical impedance technology for early cancer detection. Dr. Sanchez holds equity and serves as Scientific Advisory

Board Member of B-Secur, Ltd., a company that develops wearable ECG and impedance technology. He consults for Myolex, Inc., the company has an option to license patented surface impedance technology where the author is named an inventor. Dr. Sanchez also serves as a consultant to Impedimed, Inc., a company that develops clinical impedance technology. The company patented impedance technology where the author is named an inventor. He also serves as consultant to Texas Instruments, Inc., Happy Health, Inc., and Analog Devices, Inc., companies that develop impedance related technology for consumer use.

Acknowledgments

We appreciate Dr. Yang Li in Ningbo Institute of Technology, Beihang University for his help. This work was supported by the Friends of FSH Research (BS).

Benjamin Sanchez was supported by an Institutional Research Grant, IRG-21-131-01 Grant DOI #: 10.53354/pc.gr.151058 from the American Cancer Society. He acknowledges the direct financial support for the research reported in this publication provided by the Huntsman Cancer Foundation and the Experimental Therapeutics Program at Huntsman Cancer Institute; he also acknowledges support by the National Cancer Institute of the National Institutes of Health under Award Number P30CA042014. The content is solely the responsibility of the authors and does not necessarily represent the official views of the NIH.

9. References

- Adler A & Boyle A 2019 in 'Wiley Encyclopedia of Electrical and Electronics Engineering' Wiley pp. 1–16.
- Alix J J, McDonough H E, Sonbas B, French S J, Rao D G, Kadirkamanathan V, McDermott C J, Healey T J & Shaw P J 2020 *Clinical Neurophysiology* **131**(4), 799–808.
- Duck F A 1990 in 'Physical Properties of Tissues' Elsevier pp. 167–223.
- Faes T J C, van der Meij H A, de Munck J C & Heethaar R M 1999 *Physiological Measurement* **20**(4), R1–R10.
- Finsterer J, Fuglsang-Frederiksen A & Mamoli B 1997 *Journal of neurology, neurosurgery, and psychiatry* **63**(2), 175–80.
- Ganapathy N & Clark J 1987 *Biophysical Journal* **52**(5), 749–761.
- Gielen F L H, Cruts H E P, Albers B A, Boon K L, Wallinga-de Jonge W & Boom H B K 1986 *Medical & Biological Engineering & Computing* **24**(1), 34–40.
- Gielen F L H, Wallinga-de Jonge W & Boon K L 1984 *Medical & Biological Engineering & Computing* **22**(6), 569–577.
- Gillies A R & Lieber R L 2011 *Muscle & Nerve* **44**(3), 318–331.
- Greco E, Clark J & Harman T 1977 *Mathematical Biosciences* **33**(3-4), 235–256.
- Hamilton S J, Lionheart W R B & Adler A 2019 *Physiological Measurement* **40**(4), 044004.
- Jargal A, Seo J K & Kwon H 2020 *Journal of Elliptic and Parabolic Equations* **6**(1), 239–256.
- Jauhiainen J, Kuusela P, Seppänen A & Valkonen T 2020 *SIAM Journal on Imaging Sciences* **13**(3), 1415–1445.
- Kangasmaa O & Laakso I 2022 *Physics in Medicine & Biology* .
- Kharraz Y, Guerra J, Pessina P, Serrano A L & Muñoz-Cánoves P 2014 *BioMed research international* **2014**, 965631.
- Kim W K, Liu X, Sandner J, Pasmantier M, Andrews J, Rowland L P & Mitsumoto H 2009 *Neurology* **73**(20), 1686–1692.

- Klingler W, Jurkat-Rott K, Lehmann-Horn F & Schleip R 2012 *Acta myologica : myopathies and cardiomyopathies : official journal of the Mediterranean Society of Myology* **31**(3), 184–95.
- Klotz T, Gizzi L, Yavuz U S & Rohrle O 2020 *Biomechanics and Modeling in Mechanobiology* **19**(1), 335–349.
- Kuwabara S, Sonoo M, Komori T, Shimizu T, Hirashima F, Inaba A, Misawa S & Hatanaka Y 2008 *Muscle & Nerve* **37**(4), 426–430.
- Kwon H, de Morentin M M, Nagy J A, Rutkove S B & Sanchez B 2019 *Physiological Measurement* **40**(8), 085008.
- Kwon H, Guasch M, Nagy J A, Rutkove S B & Sanchez B 2019 *Scientific Reports* **9**(1), 3145.
- Kwon H, Nagy J A, Taylor R, Rutkove S B & Sanchez B 2017 *Physics in Medicine and Biology* **62**(22), 8616–8633.
- Liang W C & Nishino I 2011 *Current neurology and neuroscience reports* **11**(1), 97–103.
- Luo X, Gutierrez Pulido H V, Rutkove S B & Sanchez B 2021a *Clinical Neurophysiology* **132**(2), 683–687.
- Luo X, Gutierrez Pulido H V, Rutkove S & Sanchez B 2021b *IEEE Open Journal of Engineering in Medicine and Biology* **2**, 278–285.
- Luo X & Sanchez B 2021 *Physiological Measurement* **42**(4), 045009.
- Milisenda J C, Doti P I, Prieto-González S & Grau J M 2014 *Seminars in Arthritis and Rheumatism* **44**(2), 228–233.
- Nagy J A, DiDonato C J, Rutkove S B & Sanchez B 2019 *Nature Scientific Data* **6**(1), 37.
- Opitz A, Falchier A, Linn G S, Milham M P & Schroeder C E 2017 *Proceedings of the National Academy of Sciences* **114**(20), 5243–5246.
- Rush S 1962 *Journal of Research of the National Bureau of Standards, Section C: Engineering and Instrumentation* **66C**(3), 217.
- Rush S, Abildskov J A & McFee R 1963 *Circulation research* **12**(1), 40–50.
- Rutkove S B 2009 *Muscle & nerve* **40**(6), 936–46.
- Rutkove S B, Kwon H, Guasch M, Wu J S & Sanchez B 2018 *Clinical Neurophysiology* **129**(8), 1704–1708.
- Rutkove S B, Le M, Ruehr S A, Nagy J A, Semple C & Sanchez B 2022 *Muscle & Nerve* **65**(6), 702–708.
- Rutkove S B & Sanchez B 2018 *Cold Spring Harbor Perspectives in Medicine* p. a034405.
- Sanchez B, Li J, Bragos R & Rutkove S B 2014 *Physics in medicine and biology* **59**(10), 1–12.
- Sanchez B, Li J, Geisbush T, Bardia R B & Rutkove S B 2016 *IEEE Transactions on Biomedical Engineering* **63**(8), 1602–1612.
- Sanchez B, Martinsen O G, Freeborn T J & Furse C M 2021 *Clinical Neurophysiology* **132**(2), 338–344.
- Sanchez B & Rutkove S B 2017a *Neurotherapeutics* **14**(1), 107–118.
- Sanchez B & Rutkove S B 2017b *Current Neurology and Neuroscience Reports* **17**(11), 86.
- Schooling C N, Healey T, McDonough H E, French S J, McDermott C J, Shaw P J, Kadirkamanathan V & Alix J J 2022 *Clinical Neurophysiology* **139**, 69–75.
- Schwan H P 1984 *IEEE Transactions on Biomedical Engineering* **31**(12), 872–8.
- Schwan H P & Kay C F 1957 *Annals of the New York Academy of Sciences* **65**(6), 1007–13.
- Tankisi H, Otto M, Pugdahl K & Fuglsang-Frederiksen A 2013 *Muscle & Nerve* **48**(2), 296–298.
- Taylor R G & Koohmaraie M 1998 *Journal of Animal Science* **76**(11), 2811.
- Teixeira F & Chew W 1997 *IEEE Microwave and Guided Wave Letters* **7**(11), 371–373.
- Toscano A, Barca E & Musumeci O 2017 *Current opinion in neurology* **30**(5), 553–562.
- Wang Y & Pessin J E 2013 *Current opinion in clinical nutrition and metabolic care* **16**(3), 243–50.

Supplementary Material: “Electrical impedance myography method of measuring anisotropic tongue tissue”

Xuesong Luo^{1,3}, Jian Shi², Arnau Marín Llobet³, Seward B. Rutkove⁴ and Benjamin Sanchez³

¹National Engineering Laboratory for Neuromodulation, School of Aerospace Engineering, Tsinghua University, Beijing 100084, China.

²Department of Automation Science and Electric Engineering, Beijing Advanced Innovation Center for Big Data-Based Precision Medicine, Beihang University, Beijing 100083, China.

³Department of Electrical and Computer Engineering, Sorenson Molecular Biotechnology Building, 36 South Wasatch Drive, University of Utah, Salt Lake City, UT 84112, USA.

⁴Department of Neurology, Beth Israel Deaconess Medical Center, Harvard Medical School, Boston, MA 02245, USA.

Lemma 1

Consider $\mathbf{r} = (x, y, z)^T$ the vector of coordinates within the tissue Ω in half space \mathbb{R}_-^3 or full space \mathbb{R}^3 . The three-dimensional anisotropic admittivity in Ω in each direction is $\gamma_{\{x,y,z\}} \in \mathbb{C}$. A sinusoidal electrical current is externally applied with a signal amplitude $I \in \mathbb{R}$ using a current source electrode S with coordinates $\mathbf{r}_S := (x_S, y_S, z_S)^T$. The resultant electrical potential $\mathbf{U} \in \mathbb{C}$ is generated then follows the three-dimensional generalized anisotropic Poisson governing equation

$$\gamma_x \frac{\partial^2 \mathbf{U}(\mathbf{r})}{\partial x^2} + \gamma_y \frac{\partial^2 \mathbf{U}(\mathbf{r})}{\partial y^2} + \gamma_z \frac{\partial^2 \mathbf{U}(\mathbf{r})}{\partial z^2} = -I \delta(\mathbf{r} - \mathbf{r}_S) \quad (\text{A1})$$

has unique solution

$$\mathbf{U}(\mathbf{r}) = \frac{I}{K \sqrt{\det(\gamma)}} \left((\mathbf{r} - \mathbf{r}_S)^T \gamma^{-1} (\mathbf{r} - \mathbf{r}_S) \right)^{-\frac{1}{2}}, \quad (\text{A2})$$

where δ is the Dirac delta function, $\det(\cdot)$ is the determinant, γ is three-dimensional admittivity

$$\gamma = \text{diag}(\gamma_x, \gamma_y, \gamma_z) = \begin{bmatrix} \gamma_x & 0 & 0 \\ 0 & \gamma_y & 0 \\ 0 & 0 & \gamma_z \end{bmatrix}$$

and

$$K = \begin{cases} 2\pi & \Omega \text{ in } \mathbb{R}_-^3 \text{ and } \mathbf{r}_S \in \partial\Omega \\ 4\pi & \Omega \text{ in } \mathbb{R}^3 \end{cases},$$

plane $\partial\Omega$ is the boundary of half space.

Proof. Applying the idea of analytic continuation from isotropic to anisotropic problem, here we first construct the mathematical form of the solution of (A1), and then prove that (A2) is the unique result.

Consider now the three-dimensional anisotropic case [1,2]. The governing Poisson equation (A1) is now written as

$$\frac{\partial^2 \mathbf{U}(\mathbf{r})}{\partial \left(\frac{x-x_S}{\sqrt{\gamma_x}} \right)^2} + \frac{\partial^2 \mathbf{U}(\mathbf{r})}{\partial \left(\frac{y-y_S}{\sqrt{\gamma_y}} \right)^2} + \frac{\partial^2 \mathbf{U}(\mathbf{r})}{\partial \left(\frac{z-z_S}{\sqrt{\gamma_z}} \right)^2} = -I \delta(\mathbf{r} - \mathbf{r}_S) \quad (\text{A3})$$

Observing the difference between isotropic governing equation and anisotropic governing equation (A3), we can apply the idea of analytic continuation to construct the mathematical form of solution expression in three-dimensional anisotropic problem, that is

$$\mathbf{U} = C \frac{I}{K \sqrt{\gamma_x \gamma_y \gamma_z} \sqrt{\left(\frac{x-x_S}{\sqrt{\gamma_x}} \right)^2 + \left(\frac{y-y_S}{\sqrt{\gamma_y}} \right)^2 + \left(\frac{z-z_S}{\sqrt{\gamma_z}} \right)^2}} \quad (\text{A4})$$

where $C \in \mathbb{C}$ is an unknown constant.

Next we are going to prove that (A4) is the general solution to (A1). When $\mathbf{r} \neq \mathbf{r}_S$, the right hand side of (A1) is zero

$$I \delta(\mathbf{r} - \mathbf{r}_S) \equiv 0.$$

In other words, the current is only being applied at the source electrode. Simultaneously, substituting (A4) into the left hand side of (A1), i.e., $\gamma_x \frac{\partial^2 \mathbf{U}(\mathbf{r})}{\partial x^2} + \gamma_y \frac{\partial^2 \mathbf{U}(\mathbf{r})}{\partial y^2} + \gamma_z \frac{\partial^2 \mathbf{U}(\mathbf{r})}{\partial z^2}$, one can also deduce that

$$\gamma_x \frac{\partial^2 \mathbf{U}(\mathbf{r})}{\partial x^2} + \gamma_y \frac{\partial^2 \mathbf{U}}{\partial y^2} + \gamma_z \frac{\partial^2 \mathbf{U}}{\partial z^2} \equiv 0.$$

To sum up, expression (A4) satisfies governing equation (A1) in entire definitional domain. Thus, we can conclude that (A4) is the general solution to anisotropic generalized Poisson equation (A1).

According to equation (A4), C is a constant value for all possible anisotropic admittivity values. Then we can apply a specific case to determine its value. Here we give $\gamma_x = \gamma_y = \gamma_z$. From isotropic case, it can be obtained that $C = 1$. Then solution (A4) can be further simplified as

$$\mathbf{U}(\mathbf{r}) = \frac{I}{K \sqrt{\det(\boldsymbol{\gamma})}} \left((\mathbf{r} - \mathbf{r}_S)^T \boldsymbol{\gamma}^{-1} (\mathbf{r} - \mathbf{r}_S) \right)^{-\frac{1}{2}}, \quad (\text{A5})$$

which is a particular solution to governing equation (A1).

The last step is to apply the Uniqueness theorem for Poisson's equation. From the Uniqueness theorem, if one can find a solution to the boundary valued Poisson's equation problem, then that is the unique solution to this problem. Thus (A5) is the unique solution to the Poisson equation (A1) with three-dimensional (complex) anisotropic admittivity. \square

References

- [1] H. Parasuram, B. Nair, E. D'Angelo, M. Hines, G. Naldi, and S. Diwakar, "Computational modeling of single neuron extracellular electric potentials and network local field potentials using LFPsim," Frontiers in Computational Neuroscience, vol. 10, no. Jun, pp. 1–13, 2016.
- [2] H. Kwon, J. Nagy, R. Taylor, S. Rutkove, and B. Sanchez, "New electrical impedance methods for the in situ measurement of the complex permittivity of anisotropic biological tissues," Physics in Medicine & Biology, vol. 62, no. 22, p. 8616, 2017.